LANGMUIR

Article

pubs.acs.org/Langmuir

Mechanism of Particle Formation in Silver/Epoxy Nanocomposites Obtained through a Visible-Light-Assisted in Situ Synthesis

Ignacio E. dell'Erba,[†] Francisco D. Martínez,[†] Cristina E. Hoppe,[†] Guillermo E. Eliçabe,[†] Marcelo Ceolín,[‡] Ileana A. Zucchi,[†] and Walter F. Schroeder*[,†]

[†]Institute of Materials Science and Technology (INTEMA), University of Mar del Plata and National Research Council (CONICET), Juan B. Justo 4302, 7600 Mar del Plata, Argentina

[‡]Instituto de Investigaciones Fisicoquímicas Teóricas y Aplicadas (INIFTA), Universidad Nacional de La Plata, CONICET, CC 16-Suc. 4, 1900 La Plata, Argentina

Supporting Information

ABSTRACT: A detailed understanding of the processes taking place during the in situ synthesis of metal/polymer nanocomposites is crucial to manipulate the shape and size of nanoparticles (NPs) with a high level of control. In this paper, we report an in-depth time-resolved analysis of the particle formation process in silver/epoxy nanocomposites obtained through a visible-light-assisted in situ synthesis. The selected epoxy monomer was based on diglycidyl ether of bisphenol A, which undergoes relatively slow cationic ring-opening polymerization. This feature allowed us to access a full description of the formation process of silver NPs before this was arrested by the curing of the epoxy matrix. In situ time-resolved small-angle X-ray scattering investigation was carried out to follow the evolution of the number and size of the silver NPs as a function of irradiation time, whereas rheological experiments combined with near-infrared and ultraviolet−visible spectroscopies were performed to interpret how changes in the rheological properties of the matrix affect the nucleation and growth of particles. The analysis of the obtained results allowed us to propose consistent mechanisms for the formation of metal/polymer nanocomposites obtained by light-assisted one-pot synthesis. Finally, the effect of a thermal postcuring treatment of the epoxy matrix on the particle size in the nanocomposite was investigated.

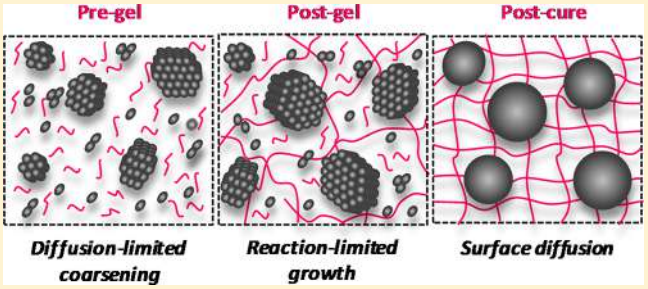

1. INTRODUCTION

Nanocomposite materials consisting of noble metal nanoparticles (NPs) dispersed in a polymer matrix offer enormous possibilities for the design of functional materials with important technological applications.[1−3] They have already been used for the development of embedded capacitors,[4] sensors,[5,6] catalysts,[7,8] conductive inks,[9] and devices for energy storage.[10] Macroscopic performance of these materials strongly depends on the possibility of homogeneously dispersing the NPs in the polymer matrix, avoiding uncontrolled aggregation phenomena that would rule out any advantages associated with the use of particles of nanoscopic dimensions. Generally, metal/polymer nanocomposites are obtained via multistep methods. Metal NPs which are first produced from the reduction of metallic precursors are then dispersed into a polymer matrix to obtain a nanocomposite material. To achieve a homogeneous dispersion, modification of the particle surface with stabilizing agents is often required to provide colloidal stability and thus prevent aggregation phenomena. A wide variety of methods of surface modification has been developed using thiols,[11,12] amines,[13] micelles,[14,15] dendrimers,[16] and polymers[17,18] as stabilization agents. Commonly, these methods require the use of very specific synthetic routes or additional time-consuming steps consisting of the replacement of the original coating by the stabilizer affine with the polymer matrix. In spite of these successful examples, increasing attention is being paid to the development of new synthetic models with facile and low-cost protocols for the preparation of metal/polymer nanocomposites with controlled morphologies and well-tuned properties.

Recently, a conceptually different methodology has been introduced for the synthesis of metal nanocomposites. This approach is based on the concomitant formation of both metal NPs and polymer matrix in the same reaction media. On the basis of this concept, several synthesis methods, either thermal or photochemical, have been developed.[19−27] In general, the thermal route yields particles with high polydispersity, thus limiting their applications as plasmonic materials. It is in this sense that the photochemical synthesis performed at room temperature has become the option of choice. In addition, the light-assisted synthesis, as compared to standard chemical approaches, provides the advantages of a uniform distribution of the reducing agent in the solution, easy modulation of the reaction rate through control on the power density, and tuning

Received: June 8, 2017
Revised: August 4, 2017
Published: September 6, 2017

DOI: 10.1021/acs.langmuir.7b01936
Langmuir 2017, 33, 10248−10258

of the wavelength to maximize the absorption by chemical species in the reaction medium.[28]

Yagci, Sangermano, and co-workers proposed a one-step photochemical approach for the preparation of metal/polymer nanocomposites.[22,25] In this case, photochemically generated free radicals reduce a silver salt to form silver NPs. As a consequence of such a redox reduction, the free radicals are concomitantly oxidized to the corresponding cations capable of initiating cationic ring-opening polymerization of epoxy monomers. In this way, spherical silver NPs homogeneously distributed in a cross-linked epoxy network were obtained. The authors also demonstrated that this method can be applicable to any other metal salts, such as gold salts, which undergo similar redox reactions with photochemically generated electron donor radicals.[24] Besides, the process is not limited only to cationically polymerizing epoxy resins. Acrylates and methacrylates that are polymerized by a free-radical mechanism can also form nanocomposites by this approach.[26]

More recently, Balan et al.[27] reported on a way of achieving certain control on the size and morphology of gold NPs in Au/urethane methacrylate nanocomposites obtained by UV-assisted one-pot one-step synthesis. The authors demonstrated that it is possible to orient the particle growth through the light power used to drive the photopolymerization reaction. Under this concept, a variety of morphologies, such as spheres, cubes, or triangular prisms, were obtained for different irradiation conditions. Other authors have also achieved some degree of control on the morphology of metal NPs by adjusting the wavelength of the light source used to drive the photochemical process.[29]

A detailed understanding of the processes taking place during the particle formation is crucial to manipulate the shape and size of NPs with a high level of control. For the light-assisted in situ synthesis, this study requires not only to capture, identify, and monitor the nucleation and growth of metal NPs during irradiation time but also to understand how diffusion constraints imposed by the matrix polymerization influence the particle formation process. To the best of our knowledge, such a study has not been addressed yet. In this work, we report an in-depth time-resolved analysis of the particle formation process in silver/epoxy nanocomposites obtained through a visible-light-assisted in situ synthesis. The selected epoxy monomer was based on diglycidyl ether of bisphenol A (DGEBA), which undergoes relatively slow cationic ring-opening polymerization.[30] This feature allowed us to access a full description of the formation process of silver NPs before this was arrested by the curing of the epoxy matrix. In situ time-resolved small-angle X-ray scattering (SAXS) investigation was carried out to follow the evolution of the number and size of silver NPs as a function of irradiation time, whereas rheological experiments combined with near-infrared (NIR) and ultraviolet−visible (UV−vis) spectroscopies were performed to interpret how changes in the rheological properties of the matrix affect the nucleation and growth of particles. The analysis of the obtained results allowed us to propose consistent mechanisms for the formation of metal/polymer nanocomposites obtained by light-assisted one-pot synthesis. The experimental evidence presented in this report is considered to be helpful for the development of reproducible processes for the in situ synthesis of metal/polymer nanocomposites with controlled morphologies and well-tuned properties.

2. EXPERIMENTAL SECTION

2.1. Materials. The epoxy monomer was based on DGEBA (DER 332, Aldrich Chemical Co.) with an epoxy equivalent weight of 174.3 g/equiv, corresponding to 0.015 hydroxyls per epoxy group. Camphorquinone (CQ), silver hexafluoroantimonate ($AgSbF_6$), and boron trifluoride ethylamine complex (BF_3·MEA) were purchased from Aldrich Chemical Co. Polyethylene glycol (PEG, average M_n = 300) was supplied by Fluka. All materials were used as received.

2.2. Preparation of Silver/Epoxy Nanocomposites. Because of the poor solubility of $AgSbF_6$ in DGEBA, the silver salt (50 mg) was first dissolved in a small amount of PEG (200 μL) at room temperature. Then, proper amounts of this solution were added to DGEBA to prepare samples containing 0.5, 1, and 1.5 wt % $AgSbF_6$. The mixtures were activated for visible-light irradiation by the addition of 2 wt % CQ and then cast onto aluminum substrates to obtain photocurable films of about 1 mm thickness. The radiation source was a light-emitting diode (LED) unit (OptoTech, Germany) with a wavelength range 410−530 nm and an irradiance equal to 427.5 mW/cm^2. The intensity of the LED was measured with the chemical actinometer potassium ferrioxalate, which is recommended for the 253−577 nm wavelength range. All irradiations were conducted at room temperature (22−25 °C).

2.3. Characterization Techniques. *2.3.1. UV−Vis Absorption Spectroscopy.* UV−vis spectra were recorded with an Agilent 8453 diode array spectrophotometer. The photoactivated mixture was contained in a thin cell constructed from two quartz slides separated by a 50 μm Teflon spacer used to regulate the sample thickness. An identical cell containing the DGEBA monomer was used as the reference. Spectra were collected immediately after each exposure interval at room temperature.

2.3.2. Fourier Transform Infrared Spectroscopy. Infrared spectroscopy was used to follow the conversion of epoxy groups as a function of irradiation time. Measurements were conducted on a Nicolet 6700 Thermo Scientific IR device in a transmission mode over the range 4000−7000 cm^{-1} from 32 coadded scans at 4 cm^{-1} resolution. The photoactivated mixtures were sandwiched between two glass plates separated by a rubber spacer of 1 mm. The specimens were irradiated at regular time intervals, and spectra were collected immediately after each exposure interval. The background spectra were collected through an empty mold assembly fitted with only one glass slide to avoid internal reflectance patterns. The same IR device provided with a heated transmission cell (HT-32, Spectra-Tech) with glass windows (32 mm diameter) and a programmable temperature controller (Omega, Spectra-Tech, $\Delta T = \pm 1$ °C) was used to monitor the consumption of epoxy groups as a function of reaction time for a neat DGEBA sample polymerized at 140 °C with BF_3·MEA as the initiator (in a ratio of 0.096 mol BF_3·MEA/mol of DGEBA). The conversion of epoxy groups was followed by measuring the height of the absorption band at 4530 cm^{-1} with respect to the height of a reference band at 4620 cm^{-1}.[31]

2.3.3. Rheometry. The evolution of the storage modulus (G') and loss modulus (G'') as a function of reaction time for a neat DGEBA sample polymerized at 140 °C with BF_3·MEA as the initiator was followed using an Anton Paar rheometer (model Physica MCR-301) provided with a CTD 600 thermochamber. A parallel-plate configuration (diameter D = 25 mm and gap H = 1 mm) was used in an oscillatory mode with 1% amplitude at a frequency of 1 Hz.

2.3.4. Small-Angle X-ray Scattering. In situ experiments were performed at room temperature on an SAXS station (beamline SAXS 1) at the National Laboratory of Synchrotron Light (LNLS, Campinas, Brazil). The reaction mixture (1 mm thick) was sealed between thin (50 μm) Kapton foils and placed in a holder mounted in the X-ray beam path so that all data were recorded at the same sample position. SAXS data were acquired for 1 s with a photoirradiation period of 10 s for the first minute of reaction. The irradiation period was then gradually increased, maintaining the same acquisition time. The scattering intensity (in arbitrary units) was recorded as a function of scattering vector $q = (4\pi/\lambda)\sin(\theta/2)$, where λ is the radiation wavelength (1.54 Å) and θ is the scattering angle. A Pilatus 300 K

DOI: 10.1021/acs.langmuir.7b01936
Langmuir 2017, 33, 10248−10258

Scheme 1. Proposed Mechanism for the One-Pot Synthesis of Silver/Epoxy Nanocomposites by Visible-Light-Induced Electron-Transfer and Cationic Polymerization Processes

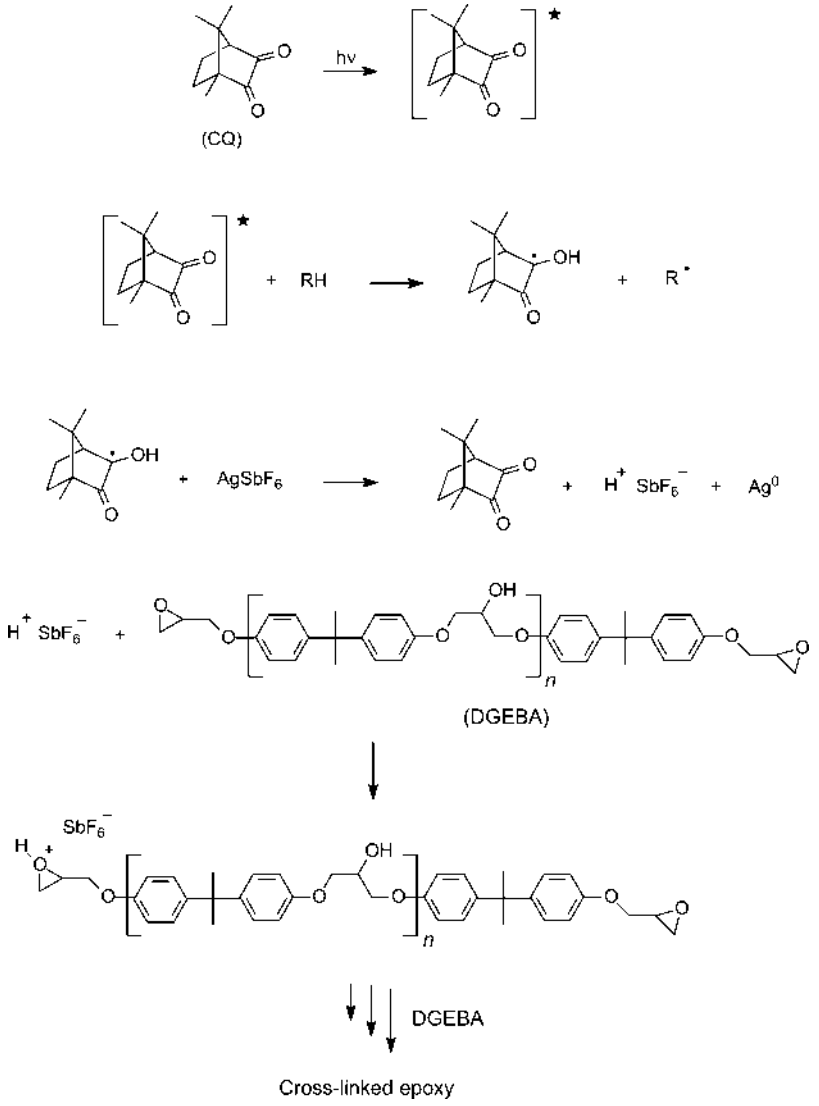

detector (Dectris, Switzerland) was used to record the SAXS patterns. The sample-to-detector distance was set to be 2500 mm. SAXS curves of cured and postcured samples were also recorded in a XEUSS 1.0 (Xenocs, Grenoble, France) system (INIFTA, project "Nanopymes", EuropeAid/132184/D/SUP/AR-Contract 331-896) equipped with a microfocus X-ray source (λ = 1.54 Å) and a Pilatus 100 K detector (Dectris, Switzerland). The sample-to-detector distance was determined to be 1354 mm. Measurements were performed at room temperature.

2.3.5. Transmission Electron Microscopy. Samples photoirradiated for 60 min were microtomed at room temperature with an LKB ultramicrotome equipped with a diamond knife. The resulting ultrathin sections (ca. 60 nm in thickness) were collected on copper grids and subsequently examined using a JEOL 100CX electron microscope operated at an accelerating voltage of 80 kV.

2.3.6. Differential Scanning Calorimetry. The calorimetric measurements were made on a PerkinElmer Pyris 1 differential scanning calorimeter under a dry nitrogen atmosphere. The sample of about 10 mg was placed in a thin-walled aluminum pan, and an empty pan of the same dimension was used as a reference. The sample was first heated from 25 to 230 °C (first heating scan) and subsequently cooled back down to 25 °C (cooling scan). Following the cooling scan, a second heating scan from 25 to 180 °C was recorded. For all scans, a rate of 10 °C/min was used. Glass-transition temperatures were defined at the onset value of the change in the specific heat during the heating scans.

2.4. SAXS Data Analysis. Experimental SAXS curves were analyzed, assuming a two-electron density model consisting of a dilute set of isolated particles embedded in a homogeneous matrix. Under such assumptions, the scattering intensity $I(q)$ in the low-q region can be written as[32]

$$I(q) = I(0)\, e^{-R_g^2 q^2/3} \tag{1}$$

which is the well-known Guinier law, where R_g is the average radius of gyration and $I(0)$ is the $\lim_{q\to 0} I(q)$, given by

$$I(0) = N(\rho_p - \rho_m)^2 V^2 \tag{2}$$

where N is the particle number, ρ_p and ρ_m are the average electron densities of the particles and the matrix, respectively, and V is the mean volume of the particles. From a logarithmic plot of eq 1 ($\ln I$ vs q^2), the average radius of gyration R_g can be derived from the slope of the straight line at small q-values. This linear plot can also be used to determine the extrapolated scattering intensity $I(0)$. Assuming spherical particles, the mean radius of the particles is related to their average radius of gyration by $R = \left(\frac{5}{3}\right)^{1/2} R_g$. Assuming furthermore that the average electron densities of the particles and the matrix (ρ_p

DOI: 10.1021/acs.langmuir.7b01936
Langmuir 2017, 33, 10248−10258

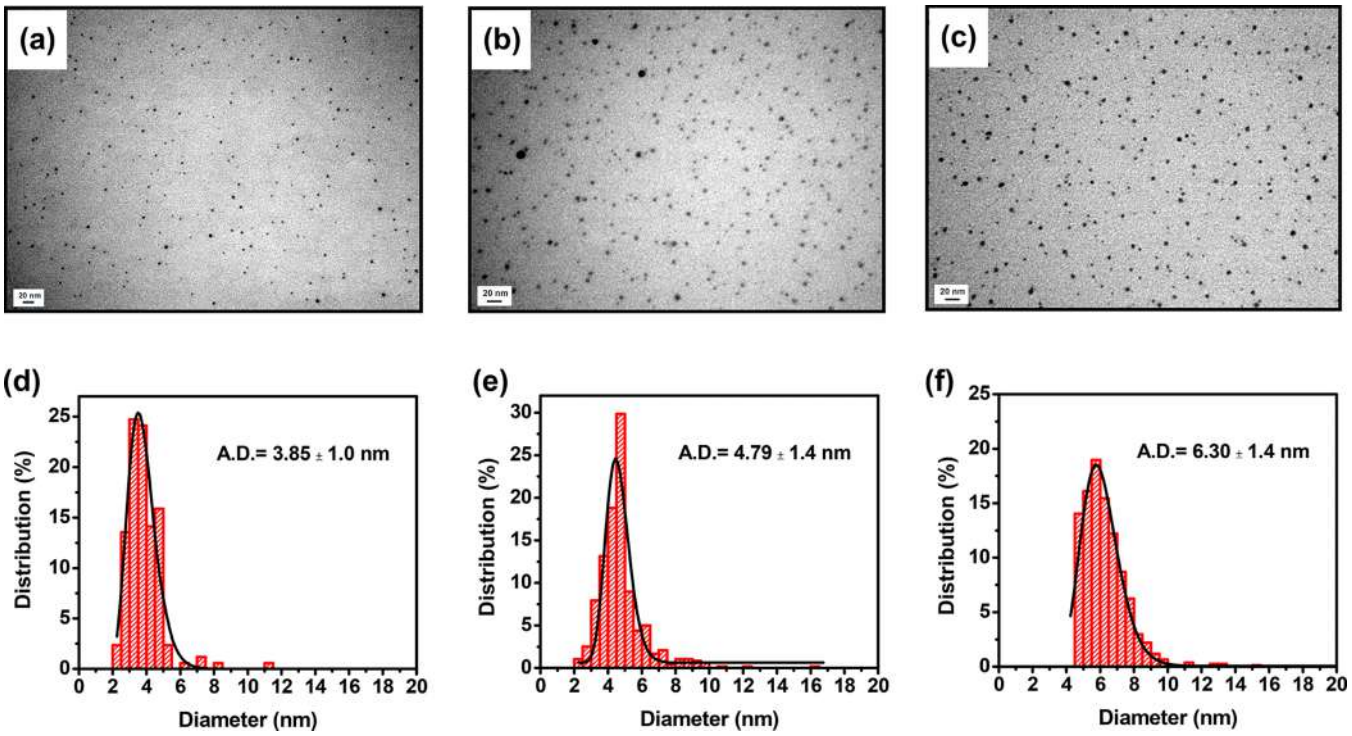

Figure 1. TEM images and particle size distributions for silver/epoxy nanocomposites obtained after 60 min of irradiation with visible light (410−530 nm, 427.5 mW/cm^2). Top: TEM images of nanocomposites obtained in the presence of different contents of silver salt: (a) 0.5, (b) 1, and (c) 1.5 wt % $AgSbF_6$. The black bars represent 20 nm. Bottom: particle size distributions extracted from the TEM images for nanocomposites obtained in the presence of (d) 0.5, (e) 1, and (f) 1.5 wt % $AgSbF_6$. The black lines represent the fitting curves with log−normal distributions.

and ρ_m) remain constant during reaction, the quotient $I(0)/V^2$ is an appropriate quantity to monitor the evolution of the particle number as a function of irradiation time (see eq 2).

To determine the particle size distribution, a polydispersed system of spherical particles was assumed. The total scattering intensity related to this system is given by[33]

$$I(q) = (\rho_p - \rho_m)^2\left(\frac{4\pi}{3}\right)^2 \int D(R)R^6\left[\frac{3[\sin(qR) - (qR)\cos(qR)]}{(qR)^3}\right]^2 dR \quad (3)$$

where $D(R)$ is the particle radius distribution function. In this work, the SASfit software package was used to calculate the particle radius distribution by solving eq 3 with the experimental scattering curves.

3. RESULTS AND DISCUSSION

3.1. Preparation of Silver/Epoxy Nanocomposites. Nanocomposite materials containing silver NPs dispersed into an epoxy matrix were prepared by visible-light-induced electron-transfer and cationic polymerization processes. Depicted in Scheme 1 is the proposed mechanism for the synthesis, where four discrete steps can be discerned.[25] In the first step, visible-light irradiation produces the excitation of CQ to its singlet, which is rapidly converted to its triplet state by intersystem crossing. The excited CQ molecule is initially reduced by a hydrogen donor (e.g., monomer or other protogenic component) to give place to the ketyl free radical which in turn reduces the silver salt to form silver NPs . The strong Brønsted acid derived from this process initiates the cationic ring-opening polymerization of epoxy monomers.

For the present study, we have selected an epoxy monomer based on DGEBA, which undergoes relatively slow cationic ring-opening polymerization.[30] This feature allowed us to access a full description of the formation process of silver NPs before this was arrested by the curing of the epoxy matrix.

The photoactivated mixtures that comprised DGEBA, $AgSbF_6$, and CQ were cast and irradiated with visible light (at 427.5 mW/cm^2, in the 410−530 nm range) at room temperature. Under these conditions, several minutes of irradiation were required to reach a high enough epoxy conversion level, as discussed in the following section. Figure 1 shows the transmission electron microscopy (TEM) images of ultrathin cuts for the epoxy thermosets cured in the presence of 0.5, 1, and 1.5 wt % of silver salt. As can be seen, the final materials showed spherical silver NPs dispersed in the epoxy matrix without any evidence of agglomeration. The XRD patterns show the characteristic peak corresponding to Ag(111) at 38°, superimposed to an amorphous halo due to the epoxy matrix (Figure S1 in the Supporting Information). The mean particle diameters obtained by TEM image analysis (using the Image-Pro Plus software) were 3.8, 4.8, and 6.3 nm for nanocomposites prepared with 0.5, 1, and 1.5 wt % of silver salt, respectively. These results show that the final size of the silver NPs is tightly related to the initial Ag^+ concentration in the reaction medium. The higher the initial Ag^+ concentration, the larger the final particle size, for the studied concentration range. The particle size distributions were properly described for log−normal distributions as represented by the black lines in Figure 1d−f. All cured samples were visually transparent (see Figure S2 in the Supporting Information). This is additional evidence that the metallic NPs are well-dispersed throughout the material without macroscopic agglomerations.

Figure 2 shows the normalized UV−vis absorption spectra of the cured samples with different silver salt contents. The spectra displayed an absorption peak centered at around 410

DOI: 10.1021/acs.langmuir.7b01936
Langmuir 2017, 33, 10248−10258

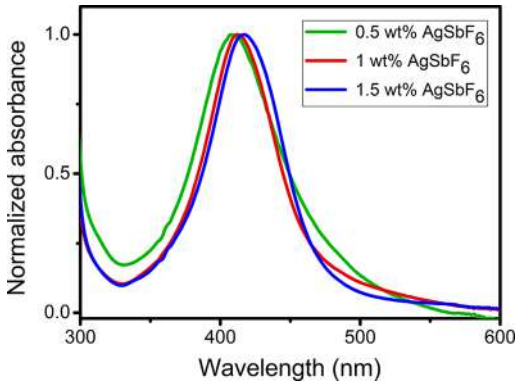

Figure 2. Normalized UV–vis absorption spectra of the epoxy nanocomposites cured in the presence of 0.5, 1, and 1.5 wt % of silver salt. The samples were irradiated for 60 min with visible light (410–530 nm and 427.5 mW/cm^2).

nm, which agrees with the characteristic surface plasmon resonance of silver NPs, commonly found between 400 and 435 nm, depending on the size, shape, and surrounding medium.[34,35] As can be noted, the plasmon peak shifted from 407 nm (for 0.5 wt % $AgSbF_6$) to 412 and 417 nm for 1 and 1.5 wt % $AgSbF_6$, respectively. This red shift is ascribed to an increase in the mean particle size with the content of silver salt, as evidenced by TEM.[35] Information about how the silver NPs are formed during visible-light irradiation is presented in a following section.

3.2. Conversion of Epoxy Groups. The progress of the polymerization was monitored by following the decrease in absorbance of the characteristic IR band of the epoxy groups centered at 4530 cm^{-1}. Figure 3 shows the conversion curves of

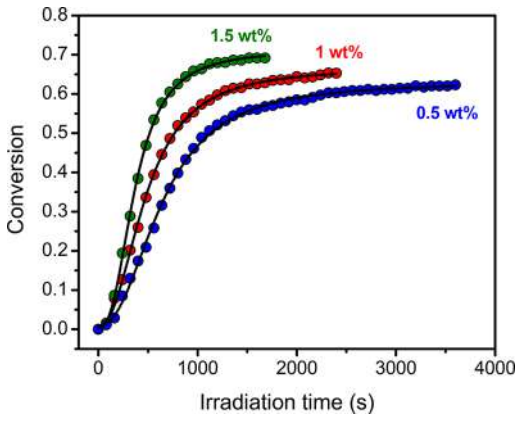

Figure 3. Conversion of epoxy groups as a function of irradiation time for the samples containing 2 wt % CQ and different concentrations of $AgSbF_6$: 0.5 wt % (blue points), 1 wt % (red points), and 1.5 wt % (green points). Irradiations were conducted with an LED unit operated in the visible region of the spectrum (410–530 nm and 427.5 mW/cm^2). Lines are drawn to guide the eye.

epoxy groups as a function of irradiation time for the samples containing 0.5, 1, and 1.5 wt % of silver salt. As can be noted, the polymerization of DGEBA was accelerated as the amount of silver salt in the reaction mixture was increased. For example, for 500 s of irradiation, the conversion of epoxy groups increased from 0.21 (for 0.5 wt % $AgSbF_6$) to 0.35 and 0.48 for 1 and 1.5 wt % $AgSbF_6$, respectively. From the kinetic studies of the cationic polymerization of epoxides,[36] it is known that the strong Brønsted acid generated rapidly protonates the epoxy groups to form oxonium ion intermediates that propagate the polymerization reaction, as shown in Scheme 1. The chain propagation steps are slow compared to the initiation reactions. On the basis of this argument, we interpret that the polymerization rate of DGEBA increases with the silver salt content as the concentration of strong Brønsted acid, and consequently that of oxonium ion intermediates, increases.

In cross-linking reactions (such as polymerization of DGEBA), the gel point is a critical transition characterized by the change of the reaction medium from a liquid state to a solid one (the viscosity tends to infinite). In the case of epoxy reactions, the characteristic time scale related to the local mobility of functional groups after gelation continues to be much shorter than the characteristic time scale to produce the chemical reaction.[37] This means that gelation does not significantly influence the kinetics of the cross-linking reaction; however, it can have a dramatic effect on the formation mechanism of silver NPs, as discussed in the next section.

To determine the gel point conversion, we analyzed a neat DGEBA sample cured by thermal cationic polymerization (at 140 °C) with BF_3·MEA as the initiator. Figure 4a shows the evolution of the dynamic storage modulus (G') and loss modulus (G'') during the first 700 s of reaction. As can be seen, the gel point took place at 330 s of reaction, as determined by the crossover of G' and G'' (a precise determination of the gel point would require to obtain the condition where $\tan \delta = G''/G'$ becomes independent of frequency; however, it is accepted that the crossover of G' and G'' provides a proper estimation of the gel point.)[38] In addition, real-time Fourier transform infrared measurements under the same reaction conditions were carried out to transform the time data of the rheological experiment into conversion data. As shown in Figure 4b, the gel point conversion was approximately 0.03. Therefore, from Figure 3, we can determine that during the preparation of nanocomposites containing 0.5, 1, and 1.5 wt % of silver salt, the gel point occurs around 60 s of irradiation.

3.3. Formation of Silver NPs during Photoirradiation. At the selected irradiation conditions, silver particle formation proceeds in a time scale that enables the monitoring by SAXS at a synchrotron radiation facility with a suitable time resolution for all studied formulations. Figure 5 shows the temporal evolution of the SAXS profiles obtained during the first 420 s of irradiation for the samples containing 0.5, 1, and 1.5 wt % of silver salt. A strong increase of scattering intensity and a major change of shape of the scattering curves within the first 60 s of irradiation can be observed for the three formulations analyzed. As can be seen, the scattering profiles displayed a smooth slope in the central part of the curve, followed by a Gaussian decay at higher q-values. This shape of the SAXS profiles is characteristic of a dilute set of noninteracting particles.[32] From 60 to 420 s of irradiation, no significant changes in the scattering curves were observed except for a small increase in the intensity, whereas for irradiation times longer than 420 s, the profiles were almost identical, indicating that all available Ag^+ precursors were consumed for particle formation and that coalescence between the already formed NPs could proceed only to a minor degree.

Information about the evolution of the mean radius and the number of particles as a function of irradiation time was obtained from the SAXS curves in the Guinier region, as described in the section 2.4. Guinier plots ($\ln I$ vs q^2) indicating the linear region used to determine R_g and $I(0)$ are depicted in the Supporting Information (Figure S3). The changes of mean

DOI: 10.1021/acs.langmuir.7b01936
Langmuir 2017, 33, 10248–10258

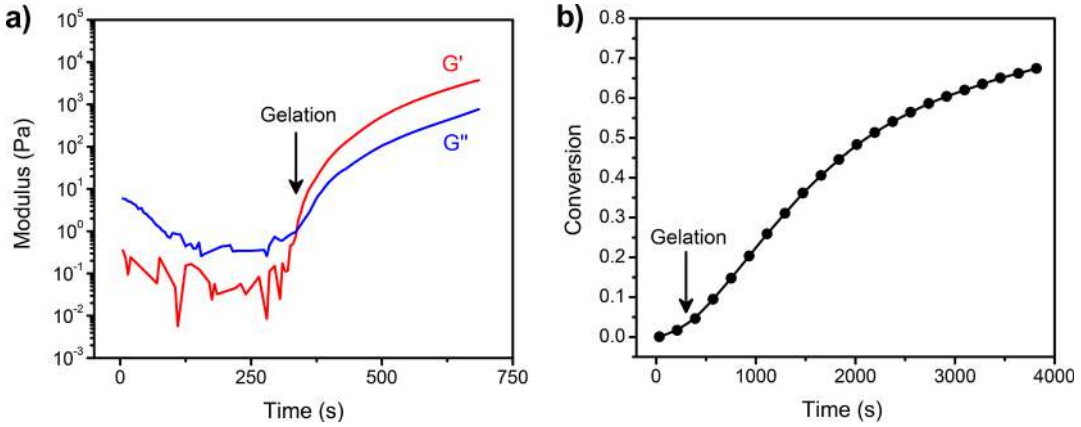

Figure 4. (a) Storage modulus (G') and loss modulus (G'') as a function of reaction time for a neat DGEBA sample cured by thermal cationic polymerization at 140 °C with BF_3·MEA as the initiator. (b) Real-time conversion profile for a neat DGEBA sample polymerized under the same reaction conditions as those used for the rheological experiment shown in (a).

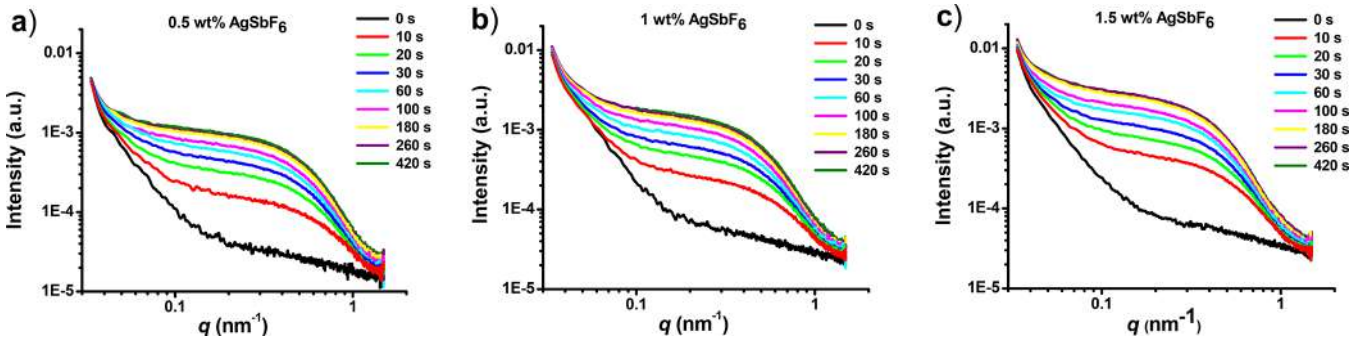

Figure 5. SAXS profiles at different irradiation times for the samples containing (a) 0.5, (b) 1, and (c) 1.5 wt % $AgSbF_6$. Irradiations were conducted with an LED unit operated in the visible region of the spectrum (410−530 nm and 427.5 mW/cm^2).

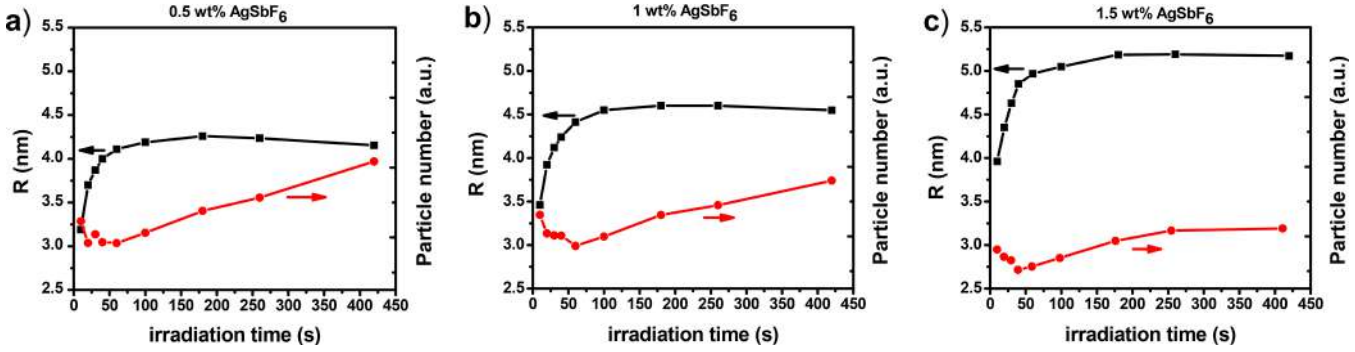

Figure 6. Evolution of the mean particle radius and particle number as a function of irradiation time for the samples containing (a) 0.5, (b) 1, and (c) 1.5 wt % $AgSbF_6$. Irradiations were conducted with an LED unit operated in the visible region of the spectrum (410−530 nm and 427.5 mW/cm^2). Lines are drawn to guide the eye.

particle radius (R), derived from R_g, assuming spherical particles [$R = (5/3)^{1/2}R_g$], together with the evolution of particle number [$I(0)/V^2$] are shown in Figure 6. Two different regimes of particle formation can be distinguished in the three formulations studied. The first one took place during the first 60 s of irradiation for all samples, where the mean radius rapidly increased with time, whereas the number of particles simultaneously decreased. Note that this period corresponds to the pregel stage of the polymerization reaction. After 60 s of irradiation (postgel stage), a second regime of the particle formation was observed, where the mean radius reached a maximum value and then slightly decreased, whereas the number of particles continuously increased.

Further information of the particle formation process was obtained by UV−vis spectroscopy. Figure 7a shows the evolution of the UV−vis absorption spectra during the irradiation time for a sample containing 1 wt % of silver salt. A rapid increase of the plasmon absorption peak was observed as a result of the Ag NP formation. To aid in the interpretation of these results, we plotted the maximum absorbance of the plasmon peak as a function of irradiation time (Figure 7b). An incubation period, where the absorbance almost did not change with time, was observed in the initial stage of irradiation (0−5 s). From 5 to 60 s of irradiation, the absorbance rapidly increased with a constant growth rate, as indicated by the red line in Figure 7b. This period coincides with the first regime of

DOI: 10.1021/acs.langmuir.7b01936
Langmuir 2017, 33, 10248−10258

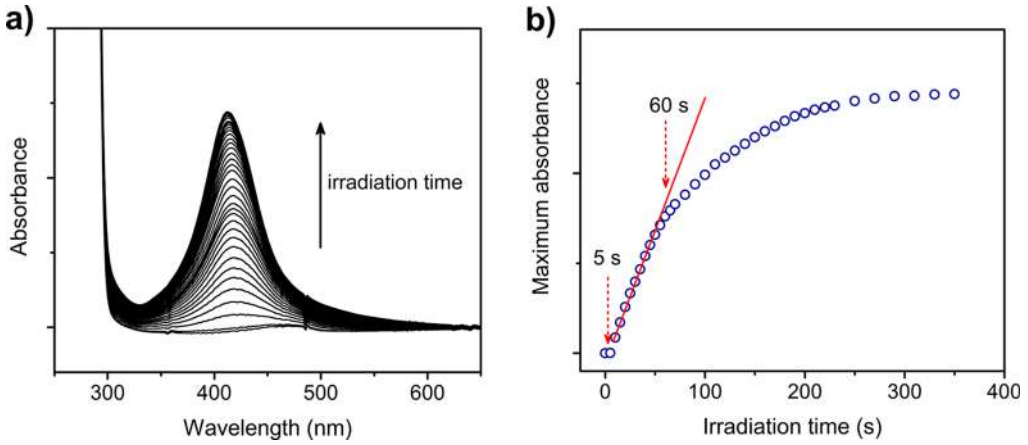

Figure 7. (a) Temporal evolution of the UV−vis absorption spectra during irradiation for a sample containing 1 wt % $AgSbF_6$. (b) Maximum absorbance of the plasmon peak as a function of irradiation time as extracted from the UV−vis absorption spectra shown in (a). Irradiations were conducted with an LED unit operated in the visible region of the spectrum (410−530 nm and 427.5 mW/cm^2).

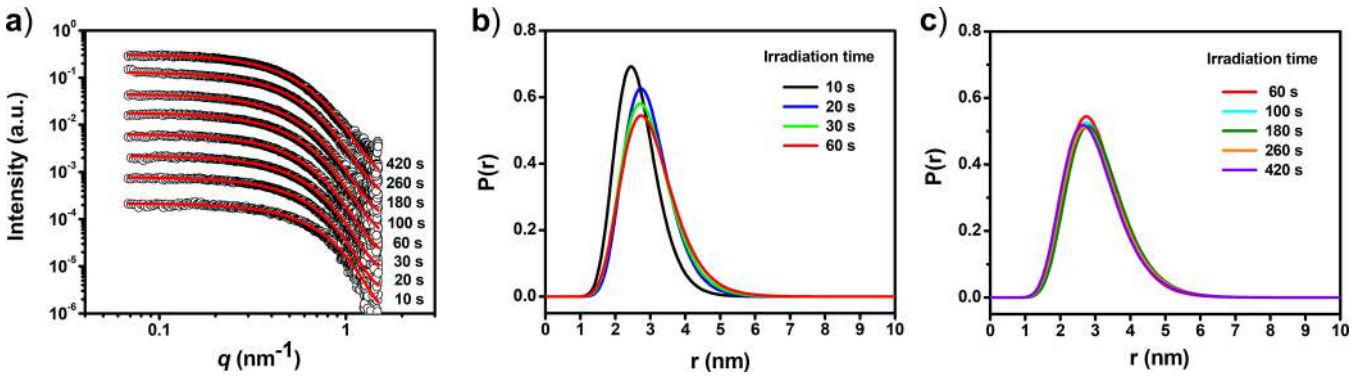

Figure 8. Analysis of the SAXS data, assuming a model of polydisperse spherical nanoobjects, for the sample with 1 wt % $AgSbF_6$. (a) Fitting of the SAXS diagrams for different irradiation times. The red solid lines are the fitting curves, and the symbols represent the experimental values. For visual clarity, the SAXS curves were shifted along the vertical axis. (b) Predicted distributions of particle sizes during the first regime of growth (up to 60 s of irradiation). (c) Predicted distributions of particle sizes during the second regime of growth (from 60 to 420 s of irradiation).

the particle formation detected by SAXS. After 60 s of irradiation (the second regime), the growth rate of the plasmon peak continuously decreased with time until finally tended to zero between 300 and 400 s of irradiation. Similar features were observed for the samples containing 0.5 and 1.5 wt % of silver salt, as shown in the Supporting Information (Figure S4). Evidently, a change in the mechanism of particle formation occurred around 60 s of irradiation, concurrently with the gelation of the epoxy matrix.

Usually, the noble metal NP formation process is described in terms of the theory of nucleation and growth.[39] For the nucleation process, it can be assumed that Ag^+ ions are first reduced to isolated Ag^0 atoms, as depicted in Scheme 1. When a critical concentration of Ag^0 atoms is achieved, formation of Ag nuclei occurs by the aggregation of these atoms. The nucleation begins at the very early stages, and it continues during the whole formation process. According to the classical nucleation theory,[40] the Ag nuclei can grow up only when the nuclei size is larger than some critical size. When this occurs, Ag nuclei growth was controlled by two mechanisms: (1) *diffusion-limited coarsening*,[41−43] which involves the collective motion of particles or nuclei that grow upon collision (dynamic coalescence) or through the transfer of atoms from smaller particles to larger particles (Ostwald ripening), and (2) *reaction-limited growth*,[39,44] where the growth occurs by the reduction of Ag^+ ions onto the surface of nuclei or particles present in the medium. A detailed understanding of the nucleation and growth processes is crucial to control the particle formation in the nanocomposite.

The results shown in Figures 6 and 7 provide valuable insights into the mechanism of particle formation. First, we can infer that the nucleation process began rapidly, over the first 5 s of irradiation, and it continued during the whole particle formation process. After 5 s of irradiation, the first regime of particle growth took place, where the mean radius rapidly increased with time, whereas the number of particles simultaneously decreased. A decrease in the number of particles suggests that larger particles were formed by the diffusion and coalescence of smaller particles. Therefore, Ostwald ripening and dynamic coalescence can be considered as the dominant mechanisms of particle growth during this regime. Around 60 s of irradiation, a change in the main mechanism of growth took place as a consequence of diffusion constraints for the motion of particles imposed by the gelation of the epoxy matrix, as demonstrated in the previous section. Consequently, after 60 s of irradiation (the second regime), the growth proceeded mainly by the reduction of Ag^+ ions onto the surface of nuclei and particles more than by the coalescence of the formed particles. Note that during the second regime, the number of particles continuously increased with time, which demonstrates

DOI: 10.1021/acs.langmuir.7b01936
Langmuir 2017, 33, 10248−10258

that nucleation continued until the end of the particle formation process.

To determine how the size distribution of silver NPs evolved with irradiation time, the SAXS curves were analyzed using the SASfit software package, assuming a model of polydisperse spherical nanoobjects. In every case, the scattering curve of the matrix (initial solution without particles) was subtracted and polydispersity was accounted using a log−normal distribution, as confirmed by TEM image analysis (see Figure 1d−f). Figure 8a shows the fitting to the experimental SAXS curves recorded at different irradiation times for the sample with 1 wt % of silver salt. As can be seen, a very good fitting of the SAXS data was achieved. The predicted evolution in particle size distribution during the first regime of growth (up to 60 s of irradiation) is shown in Figure 8b. As the irradiation time was increased, the distribution broadened and extended to a larger radius, which implies that, during this regime, particle growth occurred mainly by coalescence among particles with different sizes. This result is in excellent harmony with our previous conclusions. Figure 8c shows the predicted distributions of particle sizes during the second regime of growth (from 60 to 420 s of irradiation). Here, no significant changes in the particle size distribution were observed except for a subtle shift of the curve toward smaller particle sizes after 180 s of irradiation due to the contribution of Ag nuclei and small particles that were continuously generated. This result is in agreement with the slight decrease of mean particle radius obtained from the Guinier plots (Figure 6b). Similar features in the temporal change of particle size distribution were predicted for the samples with 0.5 and 1.5 wt % of silver salt (see Figures S5 and S6 in the Supporting Information).

In Figure 9, we compare the predicted particle size distributions at 420 s of irradiation for the three studied formulations. One can note that the calculated distributions were similar to those obtained from TEM image analysis, as shown in Figure 1d−f. These results validate our initial premise that the obtained size of Ag NPs is closely related to the initial Ag^+ concentration in the reaction medium. By increasing the initial Ag^+ concentration, larger particles are formed accompanied by a broader particle size distribution. Therefore, the silver salt concentration can be used as a versatile way to control the particle size in the nanocomposite.

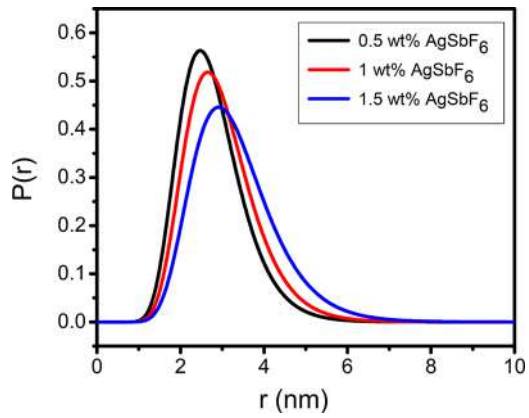

Figure 9. Predicted particle size distributions for the three studied formulations at 420 s of irradiation.

On the other hand, if a fraction of DGEBA is replaced by the respective monoepoxy monomer (i.e., phenylglycidylether), the network gelation could be delayed to a higher degree of conversion, providing more time for significant evolution of the particle size. We hypothesize that this approach could also be used as a way to control the growth processes and fine-tuning of the size of silver NPs. Work is in progress in this direction.

3.4. Thermal Postcuring of Nanocomposites. As depicted in Figure 3, the maximum conversion of epoxy groups achieved during photoirradiation at room temperature was not complete as the vitrification of DGEBA took place at a conversion value between 0.6 and 0.7. Therefore, a thermal postcuring treatment will be required to reach full conversion. The postcuring effect is assumed to be due to the activation of the still-alive reactive species when the sample is devitrified. In this section, we investigate whether the thermal treatment has any effect on the particle size in the nanocomposite.

In the first place, samples obtained by visible-light irradiation at room temperature were analyzed by differential scanning calorimetry to determine the postcuring temperature. Figure 10a shows the first DSC heating scan of the nanocomposite obtained after 60 min of irradiation, for the formulation with 1 wt % $AgSbF_6$. The sample displayed a glass transition at 51 °C, followed immediately by a broad exothermic peak due to the residual polymerization heat of DGEBA. The smaller exothermic peak that took place at a higher temperature (154 °C) can be ascribed to intra- and intermolecular transfer reactions between ether and remaining oxonium groups, which have a higher activation energy than the propagation reactions, as demonstrated by Pascault and co-workers.[45,46] Following the first DSC heating scan, the sample was cooled to room temperature, and then a second DSC heating scan was recorded (Figure 10b). In this case, there was not any residual reaction peak and T_g shifted to a higher temperature as a consequence of postcuring produced by the first heating scan.

On the basis of these results, the visible-light-cured samples were postcured at 150 °C for 1 h. Figure 11 shows the SAXS profiles obtained for the same sample (with 1 wt % of silver salt) before and after the postcuring treatment. The SAXS diagrams were analyzed using the Guinier−Porod model[47] implemented in the software package SasView 3.1.2.[48] As shown in Figure 11, a very good fitting of the SAXS data was achieved. From the fitting procedure, the average radius of gyration of the particles (R_g) and the Porod exponent (m) were extracted and are listed in Table 1.

In the framework of the Porod law ($I(q) \propto q^{-m}$),[49] for a set of particles embedded in a homogeneous matrix, the Porod exponent m is 4 for spherical particles with a smooth surface, m is between 2 and 4 for clustered particles with a rough surface, and m is 1 for rodlike particles. As seen in Table 1, for all analyzed samples, before and after the thermal postcuring treatment, the experimental value of the Porod exponent was around 4, indicating the presence of essentially spherical particles, as seen in the TEM images (Figure 1). It can also be noted that the thermal treatment produced a slight decrease in the average radius of gyration of the particles. This was an expected effect because heating promotes the diffusion of the surface atoms in partially coalesced particles, resulting in a more rounded shape, free from defects, with a lower surface energy.[41] This idea is in accord with the fact that after the thermal treatment, the Porod exponent became equal to 4.0, which corresponds to virtually perfect spherical particles. We conclude that the obtained nanocomposites can be postcured at 150 °C (epoxy matrix in the rubbery state) for 1 h without undergoing uncontrolled phenomena of particle aggregation that would

DOI: 10.1021/acs.langmuir.7b01936
Langmuir 2017, 33, 10248−10258

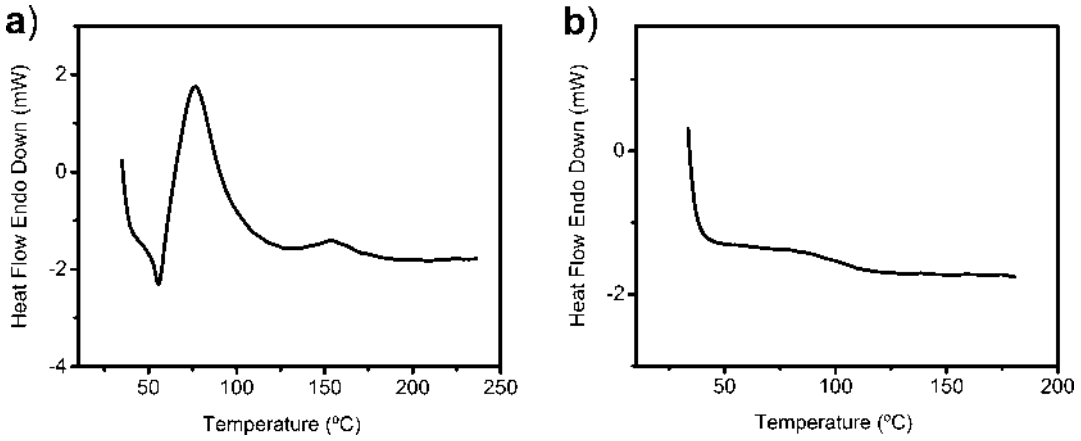

Figure 10. DSC thermograms (at 10 °C/min) for the nanocomposite formulated with 1 wt % $AgSbF_6$, obtained after 60 min irradiation with visible light (410−530 nm and 427.5 mW/cm^2): (a) first heating scan and (b) second heating scan.

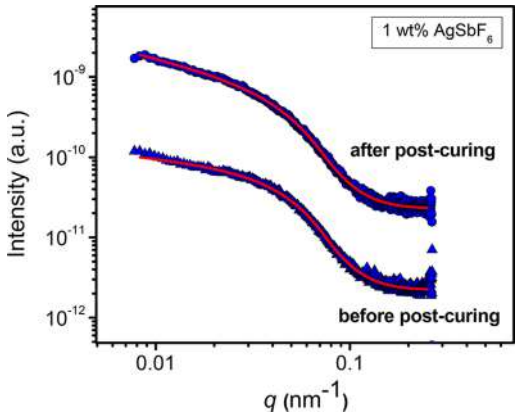

Figure 11. SAXS profiles obtained for the same sample (with 1 wt % of silver salt) before and after the postcuring treatment. The red solid lines are the fitting curves, and the blue symbols represent the experimental values. To avoid overlap, the SAXS diagrams were shifted along the vertical axis.

Table 1. Average Radius of Gyration (R_g) and Porod Exponent (m) Obtained from the Fitting of the SAXS Data Recorded before and after the Thermal Postcuring Treatment

	R_g (nm)		Porod exponent, m	
sample	cured	postcured	cured	postcured
0.5 wt % $AgSbF_6$	3.048 (±0.006)	2.817 (±0.006)	4.29 (±0.05)	4.04 (±0.04)
1.0 wt % $AgSbF_6$	3.088 (±0.007)	2.853 (±0.007)	4.18 (±0.05)	4.04 (±0.04)
1.5 wt % $AgSbF_6$	3.405 (±0.008)	3.147 (±0.007)	4.11 (±0.04)	4.05 (±0.03)

rule out any advantages associated with the use of particles of nanoscopic dimensions. Moreover, thermal postcuring could be used as a useful tool to improve the surface quality of the NPs.

4. CONCLUSIONS

The mechanism of particle formation in silver/epoxy nanocomposites obtained by visible-light-assisted one-pot synthesis has been unraveled by a combination of in situ time-resolved SAXS measurements, rheological experiments, and NIR and UV−vis spectroscopies. It has been demonstrated that nucleation begins at very early irradiation times (<5 s) and it continues during the whole particle formation process. Immediately after nucleation starts, a first regime of particle growth takes place, where the mean radius rapidly increases with time, whereas the number of particles simultaneously decreases. Ostwald ripening and dynamic coalescence can be considered as the dominant mechanisms of particle growth during this regime. When the polymerization reaction reaches the gel conversion, a change in the main mechanism of growth takes place as a consequence of diffusion constraints for the motion of particles imposed by the gelation of the epoxy matrix. At the postgel stage, the growth proceeded mainly by the reduction of Ag^+ ions onto the surface of nuclei and particles more than by the coalescence of the formed particles.

It was also demonstrated that, for the selected irradiation conditions, the obtained size of silver NPs is closely related to the initial Ag^+ concentration in the reaction medium. By increasing the initial Ag^+ concentration, larger spherical particles are formed accompanied by a broader particle size distribution. Therefore, the silver salt concentration can be used as a versatile way to control the particle size in the nanocomposite. In fact, the obtained materials can be thermally postcured without undergoing uncontrolled phenomena of particle aggregation that would rule out any advantages associated with the use of particles of nanoscopic dimensions. Moreover, thermal postcuring could be used as a useful tool to improve the surface quality of the NPs.

■ ASSOCIATED CONTENT

Supporting Information

The Supporting Information is available free of charge on the ACS Publications website at DOI: 10.1021/acs.langmuir.7b01936.

XRD profiles of both the silver/epoxy nanocomposite (formulated with 1.5 wt % $AgSbF_6$) and the neat epoxy matrix; photograph of a nanocomposite film obtained in the presence of 0.5 wt % $AgSbF_6$; Guinier plots (ln I vs q^2) indicating the linear region used to determine R_g and $I(0)$; plots showing the temporal evolution of both the UV−vis absorption spectra and the plasmon peak absorbance for the sample containing 1.5 wt % $AgSbF_6$; and fitting of the SAXS diagrams and predicted distributions of particle sizes during both the first and second regime of growth for the samples containing 0.5 and 1.5 wt % $AgSbF_6$ (PDF)

DOI: 10.1021/acs.langmuir.7b01936
Langmuir 2017, 33, 10248−10258

AUTHOR INFORMATION

Corresponding Author

*E-mail: wschroeder@fi.mdp.edu.ar.

ORCID

Cristina E. Hoppe: 0000-0002-4352-4467

Walter F. Schroeder: 0000-0002-0232-4282

Author Contributions

The manuscript was written through the contributions of all authors. All authors have given approval to the final version of the manuscript.

Notes

The authors declare no competing financial interest.

ACKNOWLEDGMENTS

The financial support of the following institutions is gratefully acknowledged: National Research Council (CONICET, Argentina), National Agency for the Promotion of Science and Technology (ANPCyT, Argentina), and University of Mar del Plata. The grant 20160198 from the Brazilian Synchrotron Light Laboratory (LNLS, Campinas-SP, Brazil) is gratefully acknowledged. M.C. is a staff researcher of CONICET, Argentina.

REFERENCES

(1) Balazs, A. C.; Emrick, T.; Russell, T. P. Nanoparticle Polymer Composites: Where Two Small Worlds Meet. *Science* **2006**, *314*, 1107−1110.

(2) Zhang, H.; Han, J.; Yang, B. Structural Fabrication and Functional Modulation of Nanoparticle-Polymer Composites. *Adv. Funct. Mater.* **2010**, *20*, 1533−1550.

(3) Habault, D.; Zhang, H.; Zhao, Y. Light-Triggered Self-Healing and Shape-Memory Polymers. *Chem. Soc. Rev.* **2013**, *42*, 7244−7256.

(4) Qi, L.; Lee, B. I.; Chen, S.; Samuels, W. D.; Exarhos, G. J. High-Dielectric-Constant Silver-Epoxy Composites as Embedded Dielectrics. *Adv. Mater.* **2005**, *17*, 1777−1781.

(5) Luechinger, N. A.; Loher, S.; Athanassiou, E. K.; Grass, R. N.; Stark, W. J. Highly Sensitive Optical Detection of Humidity on Polymer/Metal Nanoparticle Hybrid Films. *Langmuir* **2007**, *23*, 3473−3477.

(6) Jiao, S.; Jin, J.; Wang, L. One-Pot Preparation of Au-RGO/PDDA Nanocomposites and Their Application for Nitrite Sensing. *Sens. Actuators, B* **2015**, *208*, 36−42.

(7) Lu, Y.; Mei, Y.; Drechsler, M.; Ballauff, M. Thermosensitive Core−Shell Particles as Carriers for Ag Nanoparticles: Modulating the Catalytic Activity by a Phase Transition in Networks. *Angew. Chem., Int. Ed.* **2006**, *45*, 813−816.

(8) You, J.; Zhao, C.; Cao, J.; Zhou, J.; Zhang, L. Fabrication of High-Density Silver Nanoparticles on the Surface of Alginate Microspheres for Application in Catalytic Reaction. *J. Mater. Chem. A* **2014**, *2*, 8491−8499.

(9) Farahani, R. D.; Dubé, M.; Therriault, D. Three-Dimensional Printing of Multifunctional Nanocomposites: Manufacturing Techniques and Applications. *Adv. Mater.* **2016**, *28*, 5794−5821.

(10) Dhibar, S.; Das, C. K. Silver Nanoparticles Decorated Polyaniline/Multiwalled Carbon Nanotubes Nanocomposite for High-Performance Supercapacitor Electrode. *Ind. Eng. Chem. Res.* **2014**, *53*, 3495−3508.

(11) Saha, K.; Agasti, S. S.; Kim, C.; Li, X.; Rotello, V. M. Gold Nanoparticles in Chemical and Biological Sensing. *Chem. Rev.* **2012**, *112*, 2739−2779.

(12) Zheng, N.; Fan, J.; Stucky, G. D. One-Step One-Phase Synthesis of Monodisperse Noble-Metallic Nanoparticles and Their Colloidal Crystals. *J. Am. Chem. Soc.* **2006**, *128*, 6550−6551.

(13) Rak, M. J.; Saadé, N. K.; Friščić, T.; Moores, A. Mechanosynthesis of Ultra-Small Monodisperse Amine-Stabilized Gold Nanoparticles with Controllable Size. *Green Chem.* **2014**, *16*, 86−89.

(14) Grzelczak, M.; Sánchez-Iglesias, A.; Liz-Marzán, L. M. A General Approach toward Polymer-Coated Plasmonic Nanostructures. *CrystEngComm* **2014**, *16*, 9425−9429.

(15) Schöbel, J.; Karg, M.; Rosenbach, D.; Krauss, G.; Greiner, A.; Schmalz, H. Patchy Wormlike Micelles with Tailored Functionality by Crystallization-Driven Self-Assembly: A Versatile Platform for Mesostructured Hybrid Materials. *Macromolecules* **2016**, *49*, 2761−2771.

(16) Esumi, K.; Matsumoto, T.; Seto, Y.; Yoshimura, T. Preparation of Gold−, Gold/Silver−Dendrimer Nanocomposites in the Presence of Benzoin in Ethanol by UV Irradiation. *J. Colloid Interface Sci.* **2005**, *284*, 199−203.

(17) Puig, J.; Zucchi, I. A.; Hoppe, C. E.; López-Quintela, M. A.; Williams, R. J. J. A Modifier that Enables the Easy Dispersion of Alkyl-Coated Nanoparticles in an Epoxy Network. *Colloid Polym. Sci.* **2013**, *291*, 1677−1682.

(18) Stamplecoskie, K. G.; Pacioni, N. L.; Larson, D.; Scaiano, J. C. Plasmon-Mediated Photopolymerization Maps Plasmon Fields for Silver Nanoparticles. *J. Am. Chem. Soc.* **2011**, *133*, 9160−9163.

(19) Kim, J.-Y.; Shin, D.-H.; Ihn, K.-J. Synthesis of Poly(urethane acrylate-co-styrene) Films Containing Silver Nanoparticles by a Simultaneous Copolymerization/in situ Electron Transfer Reaction. *Macromol. Chem. Phys.* **2005**, *206*, 794−801.

(20) Eksik, O.; Erciyes, A. T.; Yagci, Y. In situ Synthesis of Oil Based Polymer Composites Containing Silver Nanoparticles. *J. Macromol. Sci., Part A: Pure Appl.Chem.* **2008**, *45*, 698−704.

(21) Zhang, Z.; Zhang, L.; Wang, S.; Chen, W.; Lei, Y. A Convenient Route to Polyacrylonitrile/Silver Nanoparticle Composite by Simultaneous Polymerization−Reduction Approach. *Polymer* **2001**, *42*, 8315−8318.

(22) Sangermano, M.; Yagci, Y.; Rizza, G. In Situ Synthesis of Silver−Epoxy Nanocomposites by Photoinduced Electron Transfer and Cationic Polymerization Processes. *Macromolecules* **2007**, *40*, 8827−8829.

(23) Balan, L.; Jin, M.; Malval, J.-P.; Chaumeil, H.; Defoin, A.; Vidal, L. Fabrication of Silver Nanoparticle-Embedded Polymer Promoted by Combined Photochemical Properties of a 2,7-Diaminofluorene Derivative Dye. *Macromolecules* **2008**, *41*, 9359−9365.

(24) Yagci, Y.; Sangermano, M.; Rizza, G. Synthesis and Characterization of Gold−Epoxy Nanocomposites by Visible Light Photoinduced Electron Transfer and Cationic Polymerization Processes. *Macromolecules* **2008**, *41*, 7268−7270.

(25) Yagci, Y.; Sangermano, M.; Rizza, G. A Visible Light Photochemical Route to Silver−Epoxy Nanocomposites by Simultaneous Polymerization−Reduction Approach. *Polymer* **2008**, *49*, 5195−5198.

(26) Yagci, Y.; Sangermano, M.; Rizza, G. In Situ Synthesis of Gold-Cross-Linked Poly(ethylene glycol) Nanocomposites by Photoinduced Electron Transfer and Free Radical Polymerization Processes. *Chem. Commun.* **2008**, 2771−2773.

(27) Balan, L.; Melinte, V.; Buruiana, T.; Schneider, R.; Vidal, L. Controlling the Morphology of Gold Nanoparticles Synthesized Photochemically in a Polymer Matrix through Photonic Parameters. *Nanotechnology* **2012**, *23*, 415705.

(28) Grzelczak, M.; Liz-Marzán, L. M. The Relevance of Light in the Formation of Colloidal Metal Nanoparticles. *Chem. Soc. Rev.* **2014**, *43*, 2089−2097.

(29) Stamplecoskie, K. G.; Scaiano, J. C. Light Emitting Diode Irradiation Can Control the Morphology and Optical Properties of Silver Nanoparticles. *J. Am. Chem. Soc.* **2010**, *132*, 1825−1827.

(30) dell'Erba, I. E.; Arenas, G. F.; Schroeder, W. F. Visible-Light Photopolymerization of DGEBA Promoted by Silsesquioxanes Functionalized with Cycloaliphatic Epoxy Groups. *Polymer* **2016**, *83*, 172−181.

(31) Di Luca, C.; Soulé, E. R.; Zucchi, I. A.; Hoppe, C. E.; Fasce, L. A.; Williams, R. J. J. In-Situ Generation of a Dispersion of POSS

DOI: 10.1021/acs.langmuir.7b01936
Langmuir 2017, 33, 10248−10258

Crystalline Platelets in an Epoxy Matrix Induced by Polymerization. *Macromolecules* **2010**, *43*, 9014−9021.
(32) Guinier, A.; Fournet, G. *Small-Angle Scattering of X-Rays*; Wiley: New York, 1955.
(33) Craievich, A. F. Small-Angle X-ray Scattering by Nanostructured Materials. In *Handbook of Sol-Gel Science and Technology*; Sakka, S., Ed.; Kluwer Academic Publishers: Boston, 2005; Vol. *2*, p 161.
(34) Chen, S.; Kimura, K. Water Soluble Silver Nanoparticles Functionalized with Thiolate. *Chem. Lett.* **1999**, *28*, 1169−1170.
(35) He, S.; Yao, J.; Jiang, P.; Shi, D.; Zhang, H.; Xie, S.; Pang, S.; Gao, H. Formation of Silver Nanoparticles and Self-Assembled Two-Dimensional Ordered Superlattice. *Langmuir* **2001**, *17*, 1571−1575.
(36) Bulut, U.; Crivello, J. V. Investigation of the Reactivity of Epoxide Monomers in Photoinitiated Cationic Polymerization. *Macromolecules* **2005**, *38*, 3584−3595.
(37) Pascault, J.-P.; Williams, R. J. J. General Concepts about Epoxy polymers. In *Epoxy Polymers*; Pascault, J.-P., Williams, R. J. J., Eds.; Wiley-VCH: Weinheim, 2010; p 1.
(38) Pascault, J.-P.; Sautereau, H.; Verdu, J.; Williams, R. J. J. *Thermosetting Polymers*; Dekker: New York, 2002.
(39) Turkevich, J.; Stevenson, P. C.; Hillier, J. A Study of the Nucleation and Growth Processes in the Synthesis of Colloidal Gold. *Discuss. Faraday Soc.* **1951**, *11*, 55−75.
(40) McDonald, J. E. Homogeneous Nucleation of Vapor Condensation. I. Thermodynamic Aspects. *Am. J. Phys.* **1962**, *30*, 870−877.
(41) José-Yacamán, M.; Gutierrez-Wing, C.; Miki, M.; Yang, D.-Q.; Piyakis, K. N.; Sacher, E. Surface Diffusion and Coalescence of Mobile Metal Nanoparticles. *J. Phys. Chem. B* **2005**, *109*, 9703−9711.
(42) Madras, G.; McCoy, B. J. Ostwald Ripening with Size-Dependent Rates: Similarity and Power-Law Solutions. *J. Chem. Phys.* **2002**, *117*, 8042−8049.
(43) Ratke, L.; Voorhees, P. W. *Growth and Coarsening: Ostwald Ripening in Material Processing*; Springer: Berlin, 2002.
(44) Turkevich, J. Colloidal Gold. Part I. Historical and Preparative Aspects, Morphology and Structure. *Gold Bull.* **1985**, *18*, 86−91.
(45) Bouillon, N.; Pascault, J.-P.; Tighzert, L. Epoxy Prepolymers Cured with Boron Trifluoride-Amine Complexes, 2. Polymerization Mechanisms. *Makromol. Chem.* **1990**, *191*, 1417−1433.
(46) Matějka, L.; Chabanne, P.; Tighzert, L.; Pascault, J. P. Cationic Polymerization of Diglycidyl Ether of Bisphenol A. *J. Polym. Sci., Part A: Polym. Chem.* **1994**, *32*, 1447−1458.
(47) Hammouda, B. A New Guinier−Porod Model. *J. Appl. Crystallogr.* **2010**, *43*, 716−719.
(48) This work was benefited from the use of the SasView application, originally developed under NSF award DMR-0520547.
(49) Porod, G. General Theory. In *Small-Angle X-ray Scattering*; Glatter, O., Kratky, O., Eds.; Academic Press: London, 1982; pp 17−51.

DOI: 10.1021/acs.langmuir.7b01936
Langmuir 2017, 33, 10248−10258